Broadband and omnidirectional attenuation of bulk waves in transversely isotropic soil by cross-like metamaterials

Runcheng Cai, Yabin Jin, Yan Pennec, Bahram Djafari-Rouhani, Timon Rabczuk, Xiaoying Zhuang

Journal of Applied Physics ARTICLE pubs.aip.org/aip/jap

Broadband and omnidirectional attenuation of bulk waves in transversely isotropic soil by cross-like metamaterials

Cite as: J. Appl. Phys. **136**, 243102 (2024); doi: 10.1063/5.0239151
Submitted: 17 September 2024 · Accepted: 6 December 2024 ·
Published Online: 23 December 2024

Runcheng Cai,[1,2] Yabin Jin,[3,4,a)] Yan Pennec,[2] Bahram Djafari-Rouhani,[2] Timon Rabczuk,[5] and Xiaoying Zhuang[1,6,a)]

AFFILIATIONS

[1]Department of Geotechnical Engineering, College of Civil Engineering, Tongji University, 200092 Shanghai, China
[2]Institut d'Electronique, de Microélectonique et de Nanotechnologie, UMR CNRS 8520, Département de Physique, Université de Lille, 59650 Villeneuve d'Ascq, France
[3]Shanghai Key Laboratory of Intelligent Sensing and Detection Technology, School of Mechanical and Power Engineering, East China University of Science and Technology, 200237 Shanghai, China
[4]Shanghai Institute of Aircraft Mechanics and Control, 200092 Shanghai, China
[5]Institute of Structural Mechanics, Bauhaus-Universität Weimar, Weimar D-99423, Germany
[6]Institute of Photonics, Department of Mathematics and Physics, Leibniz University Hannover, Germany

[a)]**Authors to whom correspondence should be addressed:** yabin.jin@ecust.edu.cn and zhuang@iop.uni-hannover.de

ABSTRACT

Metamaterials with bandgap properties have been widely studied and applied in the attenuation of surface and bulk waves propagating in the soil. However, most of the studies consider soil as the isotropic medium and ignore the general anisotropy property from the practical point of view. In this work, we consider the transversely isotropic constitutive model of soil and propose a cross-like metamaterial consisting of concrete inclusion and rubber coating to achieve broadband attenuation for omnidirectional bulk waves. The proposed cross-like metamaterials have more and wider bandgaps compared to circle and square metamaterials, and they have better wave attenuation performance in transversely isotropic soil with higher degrees of anisotropy. The transmission spectra of cross-like metamaterials demonstrate the wave attenuation effect of bandgaps. Furthermore, we build the full-scale transmission model considering the subway tunnel condition and demonstrate the practical wave attenuation performance of cross-like metamaterials in frequency and time domains. We also find that a larger depth of the metamaterial region will enhance wave attenuation in the bandgaps while considering rubber viscosity can enhance wave attenuation in the overall frequency ranges. The variations of omnidirectional bandgaps with rubber thickness, geometric parameters, and hollow concrete sizes are discussed. This study presents an appropriate way to design metamaterials for broadband omnidirectional bulk wave attenuation in transversely isotropic soil, which can be easily extended to other anisotropic media.

I. INTRODUCTION

Mechanical vibrations at low frequencies, stemming from traffic, equipment, or construction activities have become a significant concern in modern cities. These vibrations can not only lead to damage to architecture but also impact the performance of delicate instruments and the daily lives of residents. Traffic and engineering activities typically generate two primary types of waves: bulk waves that propagate beneath the ground and surface waves that propagate along the ground surface. Bulk waves can be classified into longitudinal waves and transverse waves as is well-known, and surface waves are generally classified into Rayleigh-like and shear modes according to their polarization with respect to the sagittal plane.[1] Surface waves have a greater impact on human society

located on the ground surface, in which Rayleigh waves travel close to the ground surface and carry most of the vibration energy, which manifests itself as the emphasis in the seismic and vibration study.

Mitigating the harmful impacts of low-frequency elastic waves remains a challenging issue in both scientific studies and engineering practices. In recent years, the thriving development of phononic crystals and metamaterials[2–5] has provided novel methods to control elastic waves in ways beyond natural materials, such as cloaking,[6–8] wave isolation and absorption,[9–11] topological insulators,[12–14] and enhanced sensitivity,[15–18] among others. In particular, seismic metamaterials have been widely studied and used to isolate or attenuate seismic waves and Rayleigh surface waves.[19–27] Various seismic metamaterials with different geometries and configurations have been proposed, and their vibration isolation and attenuation performances are investigated and demonstrated by simulations and experiments.

Compared with surface waves and seismic metamaterials, there are relatively few studies on vibration reduction and isolation metamaterials for bulk waves caused by underground vibration sources such as operating subways. Jiang *et al.*[28] studied the vibration attenuation properties of several periodic underground barriers, including circular piles, continuous walls, and multi-layer piles, considering the viscoelastic material model, and found that multi-layer piles have the best performance. Meng *et al.*[29] investigated the vibration mitigation properties of periodic pile barriers in saturated soil, and the effects of the saturated soil parameters as well as the geometric parameters of the pile on the wave attenuation were discussed. Meng *et al.*[30] further studied the vibration mitigation properties of periodic in-filled pipe pile barriers in saturated soil, and the effect of rubber viscosity was revealed. Liu and Yu[31] presented a deep-learning model to design two-dimensional periodic wave barriers distributed in a square lattice in the soil considering different site conditions. In addition, some studies have used metamaterials as the foundations of buildings or fuel storage tanks, namely, metafoundations,[32,33] providing new ideas for reducing vibration at the bottom. Although there are some studies about bulk wave attenuation metamaterials, broadband attenuation for omnidirectional bulk waves in the soil needs to be promoted.

In the studies of wave attenuation by metamaterials, most works consider soil as the linear elastic single-phase medium, which simplifies the calculation and simulation. However, from a practical point of view, the properties of ground soil are very complicated. Although there are some works considering the layered and saturated properties,[34–38] they still regard the soil as an isotropic medium, whereas natural soil is anisotropic generally. There is little research on wave attenuation metamaterials considering the anisotropic constitutive models of soil, such as the transversely isotropic constitutive model,[39–41] which is a relatively common model for anisotropic soil and characterizes the geological behavior of the earth due to sediment stratifications. Ji and Yu[42] proposed a T-shaped, partially embedded periodic barrier for surface wave attenuation in transversely isotropic soil, and they found that the bandgaps are wider in transversely isotropic soils than those in isotropic soils. Guo and Chen[43] studied the energy attenuation of shear horizontal waves in a transversely isotropic half-space with an overlying layer coupled with seismic resonators. They found that the two additional shears moduli will influence the dispersion behavior of metamaterials. However, there are few studies on bulk wave attenuation metamaterials in transversely isotropic soil, especially in soil with large anisotropy. Therefore, it is meaningful to develop the bulk wave attenuation metamaterials considering the anisotropic properties and explore the effects of the degree of soil anisotropy on the wave attenuation performance of the metamaterials.

In this work, we propose a cross-like metamaterial consisting of concrete inclusion and rubber coating to achieve broadband attenuation for omnidirectional bulk waves in transversely isotropic soil. Although some works have investigated the Lamb wave bandgap properties of metamaterials with cross-like scatters,[44–46] the bandgap properties of ternary cross-like metamaterials in the transversely isotropic medium remain unclear. We found that the proposed cross-like metamaterials have better wave attenuation performance in the soil with larger anisotropy, which has not been reported to our knowledge. The outline of the paper is as follows: In Sec. II, the metamaterial models and the band structure calculation method are presented. In Sec. III, the band structures and transmission spectra are calculated. In Sec. IV, the full-scale transmission calculations are performed. In Sec. V, the variations of bandgaps with different parameters are investigated. Finally, the conclusions are stated in Sec. VI.

II. METAMATERIAL MODELS AND BAND STRUCTURE CALCULATION METHOD

In this work, rubber-concrete metamaterials are arranged in the subway rail train vibration propagation path to attenuate the elastic waves and protect adjacent underground and above-ground architectures, as shown in Fig. 1. It is worth noting that the metamaterials are placed in the wave-propagating path between the vibration source and the protected structure. If the structure is directly above the vibration source, the metamaterials can be placed at the bottom of the structure, which is like metafoundations. The metamaterials consist of concrete inclusion and external rubber

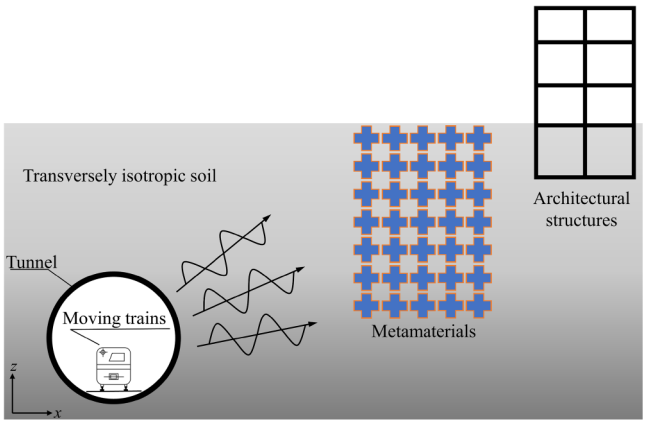

FIG. 1. Schematic of metamaterials attenuating omnidirectional elastic waves in transversely isotropic soil caused by subway rail trains.

TABLE I. Material parameters.

	ρ_s (kg/m^3)	E_v (MPa)	n
Transversely isotropic soil	2000	33.3	2
	G_v (MPa)	μ_h	μ_{vh}
	10	0.25	0.25
Concrete	ρ (kg/m^3)	E (GPa)	ν
	2500	40	0.25
Rubber	ρ (kg/m^3)	E (MPa)	ν
	1300	0.12	0.47

coating. Their density ρ, Young's modulus E, and Poisson's ratio ν are listed in Table I. It is assumed that the materials are tightly bonded between the interfaces. We investigate the wave propagation properties of metamaterials of a square lattice with three different geometries, namely, circle, square, and cross-like geometries, as shown in Fig. 2, with the lattice constant of the unit cell being $a = 1$ m.

In the absence of damping and body forces, the governing equation of elastic waves in the elastic medium can be written as[42]

$$\nabla \cdot (C(r):\nabla u(r, t)) = \rho(r)\frac{\partial^2 u(r, t)}{\partial t^2}, \tag{1}$$

where ∇ is the differential operator, $r = (x, z)$ is the position vector, t is the time, $C(r)$, $u(r, t)$, and $\rho(r)$ are, respectively, the elastic stiffness tensor, displacement vector, and mass density of the medium.

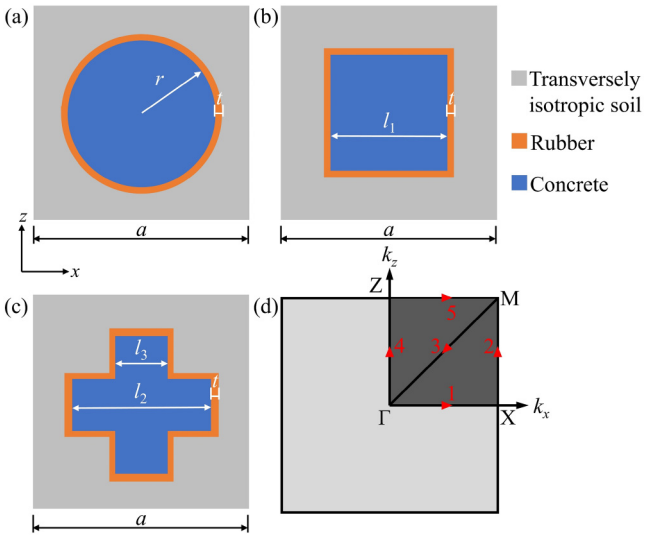

FIG. 2. Schematic diagrams of the circle (a), square (b), and cross-like (c) unit cell, and the corresponding Brillouin zone (d). The red arrows indicate the sweeping wave vectors.

Considering that the soil has transverse isotropy along the z direction, in the Cauchy coordinate system as shown in Fig. 2, its two-dimensional constitutive relations can be expressed as[39,40]

$$\sigma_x = C_{11}\frac{\partial u_x}{\partial x} + C_{13}\frac{\partial u_z}{\partial z}, \tag{2}$$

$$\sigma_z = C_{13}\frac{\partial u_x}{\partial x} + C_{33}\frac{\partial u_z}{\partial z}, \tag{3}$$

$$\tau_{xz} = C_{44}\left(\frac{\partial u_x}{\partial z} + \frac{\partial u_z}{\partial x}\right), \tag{4}$$

where elastic coefficients $C_{11} = \lambda n(1 - n\mu_{vh}^2)$, $C_{13} = \lambda n\mu_{vh}(1 + \mu_h)$, $C_{33} = \lambda(1 - \mu_h^2)$, $C_{44} = G_v$, $\lambda = E_v/[(1 + \mu_h)(1 - \mu_h - 2n\mu_{vh}^2)]$, and $n = E_h/E_v$. μ_h and μ_{vh} are Poisson's ratio characterizing the lateral strain due to the stress acting parallel and normally to the transversely isotropic medium plane, respectively. E_h, E_v, and G_v represent the horizontal Young's modulus, vertical Young's modulus, and vertical shear modulus, respectively. The parameters of transversely isotropic soil used in the study are listed in Table I.[39]

For an ideal infinite periodic system, according to the Bloch–Floquet theory, the unit cell displacement field satisfies

$$u(r + a, t) = u(r, t)e^{ik\cdot a}, \tag{5}$$

where $k = [k_x, k_z]$ is the wave vector in the Brillouin zone. The Floquet boundary conditions are applied to the four sides of the unit cell. Substituting Eq. (5) into Eq. (1) leads to the generalized eigenvalue equation which is an implicit function of the wave vector,

$$|K(k) - \omega^2 M(k)| = 0, \tag{6}$$

where $K(k)$ and $M(k)$ are stiffness and mass matrices, respectively. For a given wave vector, the eigenfrequencies ω can be obtained by solving Eq. (6). The finite element method is applied to calculate the eigenfrequencies and eigenvectors by sweeping the wave vectors along the edge of the first irreducible Brillouin zone [Fig. 2(d)]. Different from the isotropic medium, the material properties and wave propagation characteristics of the transverse isotropic medium strongly depend on the spatial direction. Consequently, the first irreducible Brillouin zone of the transverse isotropic medium should contain all directions, as shown by the dark region in Fig. 2(d). The band structures are obtained by sweeping the wave vectors along the Γ-X-M-Γ-Z-M directions, as indicated by the red arrows in Fig. 2(d).

To validate the correctness of the present numerical method for calculating the band structures, we reconsider the example studied in Ref. 47. In this work, Huang and Shi investigated the horizontal vibration mitigation property of periodic pile barriers. Figure 3 compares the band structures obtained by the present method (blue dots) and in the reference (red dots), and it is clear that a good agreement is found. Therefore, the accuracy of the present numerical method is validated.

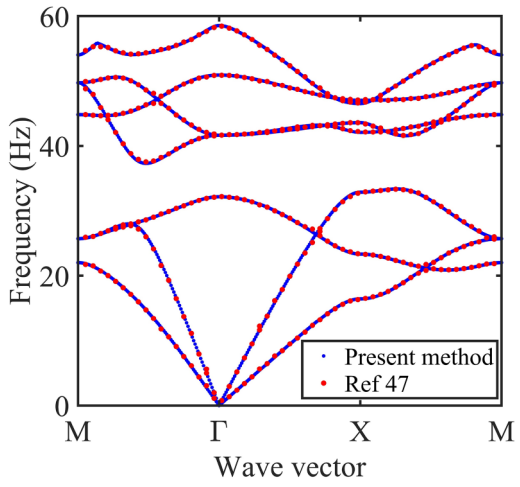

FIG. 3. Comparison of the band structures obtained by the present method (blue dots) and in Ref. 47 (red dots).

III. BAND STRUCTURES AND TRANSMISSION SPECTRA

In this section, band structures of three kinds of metamaterials with different soil anisotropic parameters are studied. The transmission spectra of cross-like metamaterials along the ΓX and ΓM directions are calculated.

In the study, thickness t of the rubber coating is 2.5 cm in three cases. For circle metamaterials, the radius of the circle concrete is 0.4 m, with a filling ratio of 50.3%. We fix the filling ratio of concrete as 50.3% and calculate the geometry parameters of square and cross-like metamaterials. The side length l_1 of the square concrete is 0.709 m, and the lengths l_1 and l_2 of the cross-like concrete are, respectively, 0.9 and 0.346 m. The band structures of three kinds of metamaterials are calculated and shown in Figs. 4(a)–4(c). For circle metamaterials, there are two omnidirectional bandgaps as indicated by the grey regions in Fig. 4(a). The lower bandgap lies between the third and fourth bands in the frequency range of 27.1–28.9 Hz with a normalized bandgap width of 6.4%. The upper bandgap extends from 65.6 to 74.6 Hz and the normalized bandgap width is 12.8%. Replacement of the circle concrete by the square concrete results in a single omnidirectional bandgap between the third and fourth bands in the frequency range of 28.5–31.4 Hz with a normalized bandgap width of 9.7%. The detailed bandgap frequency range and the normalized width of different metamaterials can be found in Table II. For cross-like metamaterials, there are four omnidirectional bandgaps in the studied range as shown in Fig. 4(c). The bandgap frequency range and the normalized bandgap width of cross-like metamaterials are summarized in Table II, where the second bandgap is quite large with a bandgap frequency range of 46.7–80.8 Hz and a normalized bandgap width of 53.5%. It is also noticed that the second and third bandgaps are almost connected because the seventh band is nearly flat.

To further investigate the wave attenuation performance of metamaterials, we calculate the complex band structures of cross-like metamaterials. We substitute Eq. (5) into Eq. (1) to get the control equations relating $\boldsymbol{k}$ and ω,

$$(\nabla + ik) \cdot (C(r):(\nabla + ik)u_k(r, t)) = \rho(r)\frac{\partial^2 u_k(r, t)}{\partial t^2}. \quad (7)$$

The complex wave numbers are solved by sweeping the angular frequency in the desired range, namely, the $k(\omega)$ method.[30,34,48,49] We utilize the coefficient form partial differential equation (PDE) (c) module in the COMSOL MULTIPHYSICS to numerically solve the implicit control equations.

The complex band structures of the cross-like metamaterials along the ΓX direction are shown in Figs. 4(d) and 4(e), where the black hollow dots represent the results obtained from the $\omega(k)$ method. The data points are colored according to their imaginary parts, while the blue (red) dots with zero (large) imaginary parts represent the propagating (evanescent) waves. A good agreement between the blue and black hollow dots is found. On the other hand, the imaginary parts in the bandgap region are larger than 0 as seen in Fig. 4(e). These results also demonstrate the correctness of the proposed $k(\omega)$ method.

The above results imply that the cross-like metamaterials are favorable to opening more and larger bandgaps that have potential practical applications. To understand the mechanism of the bandgaps, we show the vibration mode shapes at the edges of the first and second bandgaps in Fig. 4(f). The lower edge mode A of the first bandgap manifests itself as the torsional mode in scatterers with the most energy located in the concrete inclusion, which demonstrates the local resonance of the rubber-concrete element. In addition, the mechanisms of the first bandgap of the circle and square metamaterials are also the local resonance of the rubber-concrete element. The upper edge mode B of the first bandgap and the upper edge mode D of the second bandgap manifest the resonant modes of the surrounding soil, where modes B and D are, respectively, the torsional and quadrupolar modes in the matrix. It is worth noting that the square lattice of the cross-like metamaterials also implies a periodic arrangement of the square soils connected by the narrow connectors. The mechanisms of the wider second bandgap are the local resonance of the square soils connected by the narrow connectors.[46] For the lower edge mode C of the second bandgap, the displacement is located in the rubber coating and its surrounding media, which is more likely the coupling mode between scatters and matrix.

To illustrate the influence of the transversely isotropic parameter n on the metamaterial properties, a general analysis is performed here. For transversely isotropic soil, the values of $0.5 \leq n \leq 3$ are reasonable.[39,50] We show the band structures of three kinds of metamaterials when n is 2 in Fig. 4, and the results when n is 1 and 3 are shown in Fig. 5, where the larger the parameter n, the stronger the degree of anisotropy. For the circle metamaterials shown in Fig. 5(a), the first bandgap has almost no change under three different parameters due to the mechanism of local resonance. This variation also appears for the first bandgap of square metamaterials [Fig. 5(b)] and the first and second bandgaps of cross-like metamaterials [Fig. 5(c)]. However, the second bandgap of circle metamaterials gradually narrows with the increasing parameter n (namely, increasing anisotropy). On the contrary, for

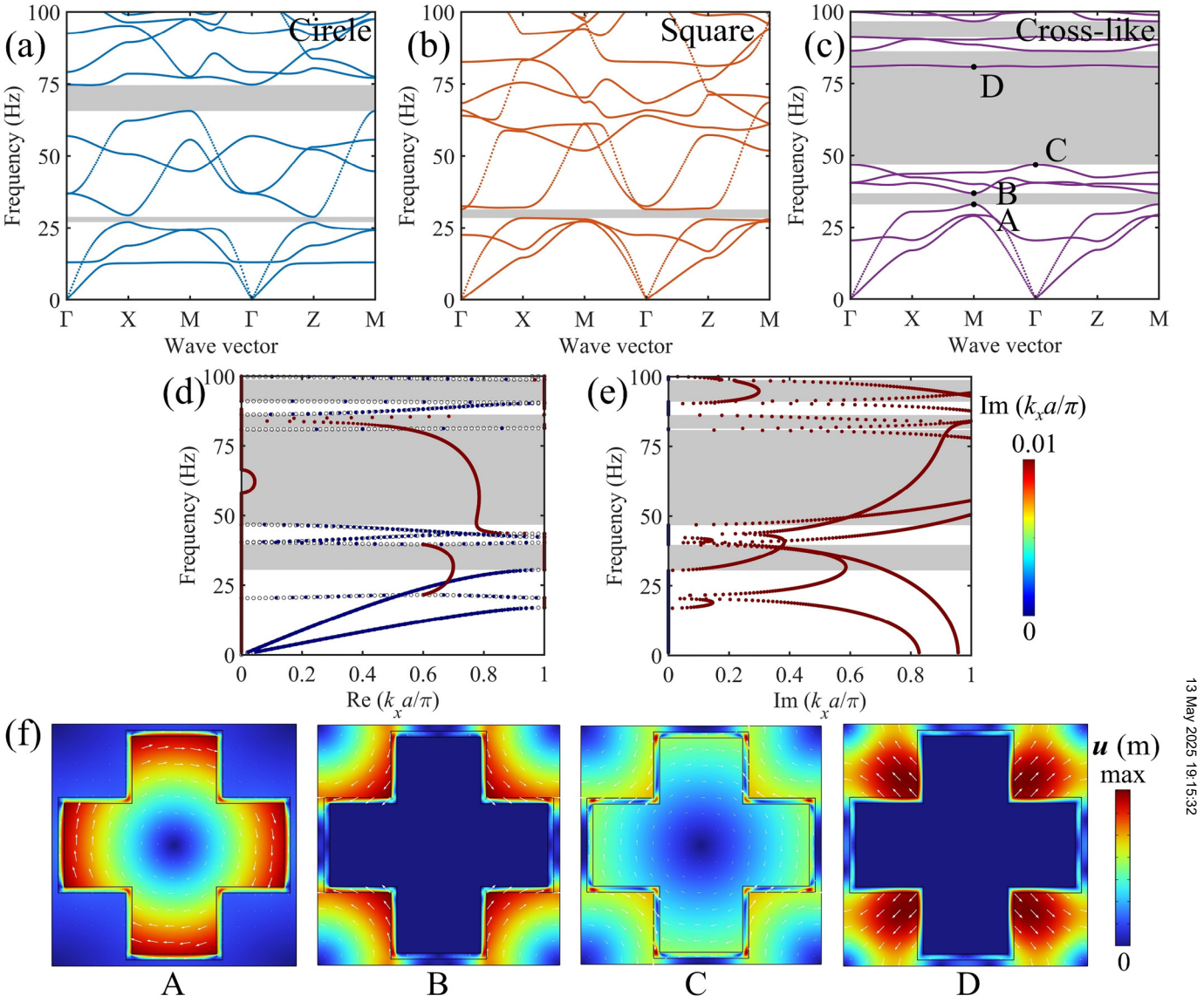

FIG. 4. Band structures of circle (a), square (b), and cross-like (c) metamaterials. The gray regions indicate the omnidirectional bandgaps. Real (d) and imaginary (e) parts of complex band structures along the ΓX direction corresponding to (c). The black hollow dots in (d) represent the results of (c). The data points are colored according to their imaginary parts. (f) The mode shapes correspond to the points A, B, C, and D in (c). The color scale in (f) represents the total displacement. The arrows indicate the displacement field.

cross-like metamaterials shown in Fig. 5(c), it is noted that the third and fourth bandgaps appear and widen with the increasing parameter n. These results demonstrate that the degree of soil anisotropy has an impact on the properties of metamaterials. A larger soil anisotropy has a positive effect on the opening and widening bandgaps of cross-like metamaterials but has a negative effect on circle metamaterials. In the following studies, we fix the parameter n being 2 and focus on cross-like metamaterials.

The band structures imply the wave characteristics of the ideal infinite periodic system, while the metamaterials for practical applications are of limited size. Therefore, it is necessary to calculate the transmission spectra of the finite periodic metamaterials in the frequency domain to assist in characterizing the wave propagation characteristics of the metamaterials. Metamaterials have different responses to incident waves from different directions. Here, we calculate the transmission spectra of the metamaterials along the ΓX

TABLE II. Frequency range and normalized width of bandgaps for different metamaterials.

Circle	First bandgap	Second bandgap	Square	First bandgap
Frequency range	27.1–28.9 Hz	65.6–74.6 Hz	Frequency range	28.5–31.4 Hz
Normalized width	6.4%	12.8%	Normalized width	9.7%
Cross-like	First bandgap	Second bandgap	Third bandgap	Fourth bandgap
Frequency range	33.0–36.8 Hz	46.7–80.8 Hz	81.3–86.1 Hz	91.1–96.6 Hz
Normalized width	10.9%	53.5%	5.7%	5.9%

and ΓM directions, which correspond to the normal incidence and 45° oblique incidence of elastic waves, respectively.

The transmission calculation models are shown in Fig. 6. For the transmission calculation model along the ΓX direction as shown in Fig. 6(a), the unit cells of the metamaterials are arranged along the x direction with the total length of l_m. The line excitation loads along the x and z directions are applied on the left of the metamaterials to excite in-plane S waves and P waves simultaneously, and the amplitudes of the loads along the x and z directions are the same. Low-reflecting boundary conditions are applied on the left and right boundaries of the model to avoid the wave reflection of the boundaries. The periodic boundary conditions are applied on the upper and lower sides of the model to simulate the periodicity of the metamaterials in the normal incident direction. To characterize the attenuation characteristics of the metamaterials to incident elastic waves, the transmission attenuation coefficient is defined as $20\lg(\Omega_1/\Omega_2)$, where Ω_1 and Ω_2, respectively, represent the total displacement (namely, $\sqrt{|u|^2+|w|^2}$) integral of the black area Q in Fig. 6 with and without metamaterials. A transmission attenuation coefficient less than 0 indicates that the metamaterials can attenuate the propagation of elastic waves, and the smaller the

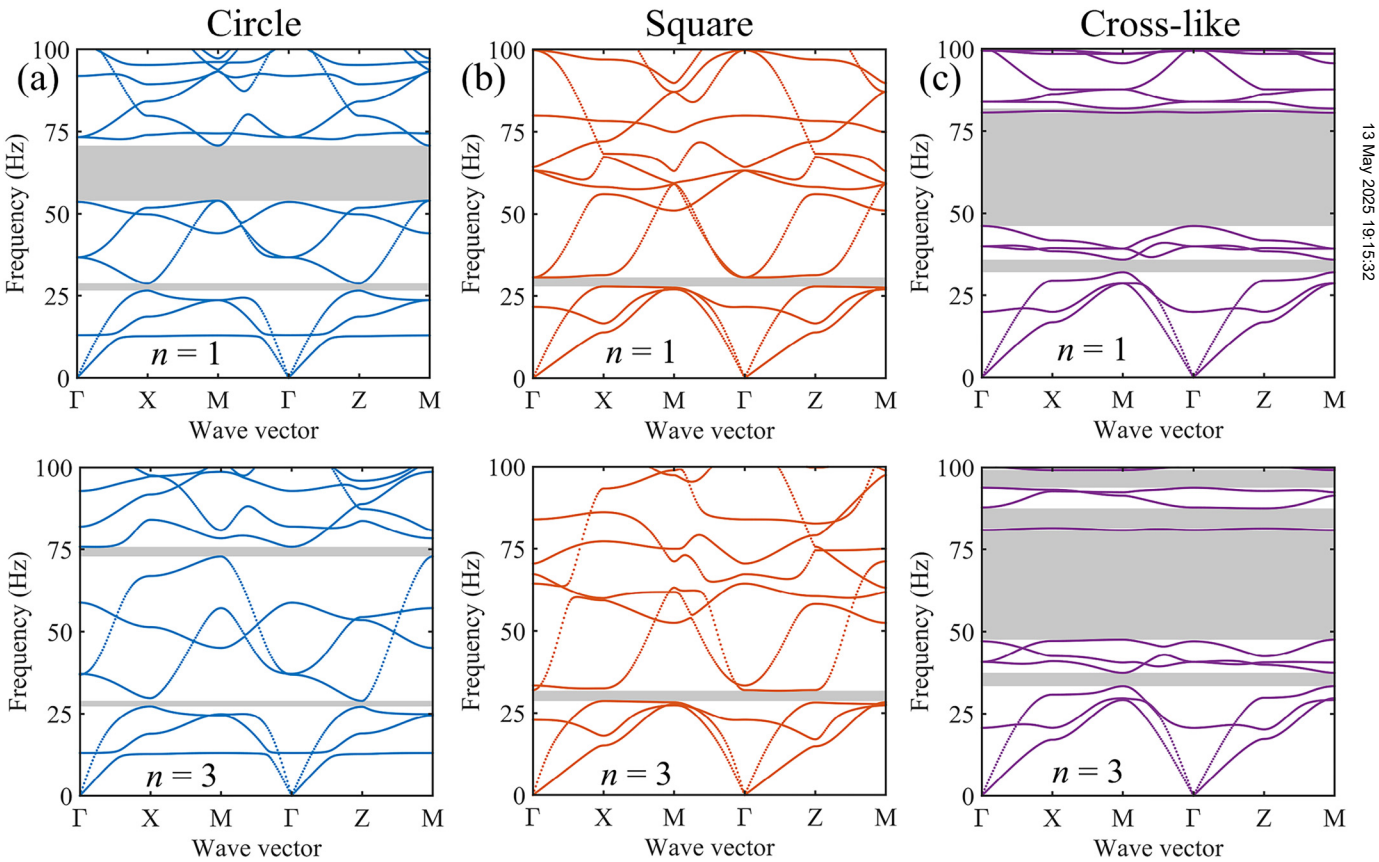

FIG. 5. Band structures of circle (a), square (b), and cross-like (c) metamaterials for different soil transversely isotropic parameter n.

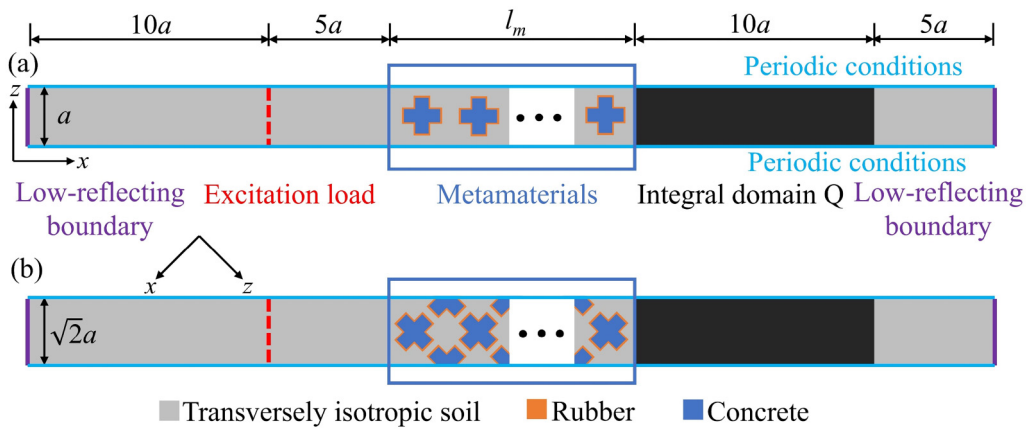

FIG. 6. Transmission calculation models along ΓX (a) and ΓM (b) directions.

transmission attenuation coefficient, the better the attenuating effect of the metamaterials.

The transmission calculation model along the ΓM direction is slightly different from that along the ΓX direction. The main difference is the arrangement of the unit cells. As shown in Fig. 6(b), the unit cells are arranged diagonally at 45°, and the width of the model becomes $\sqrt{2}$a. Unlike the isotropic medium, the elastic wave-propagating direction in the transversely isotropic medium must be consistent with the spatial coordinates. In this case, the overall model also needs to maintain an angle of 45° with the horizontal direction, as shown by the coordinate axis in Fig. 6(b).

For elastic waves propagating along the ΓX direction, the band structures and transmission spectra are shown in Figs. 7(a) and 7(b), respectively. There are four bandgaps, where the second bandgap is the largest and the same as the second omnidirectional bandgap with a bandgap frequency range of 46.7–80.8 Hz and a normalized bandgap width of 53.5%. The transmission spectra with different lengths l_m of metamaterials are calculated and shown in Fig. 7(b). The transmissions decrease significantly in the four bandgaps, especially in the second and third bandgaps, where the attenuation coefficients are less than −80 dB in most frequency ranges, indicating that elastic waves can hardly propagate through the metamaterials. The length of the metamaterials plays an important role in wave propagation, where the larger the length, the smaller the transmission in the bandgaps.

For elastic waves propagating along the ΓM direction, the band structures and transmission spectra are shown in Figs. 7(c) and 7(d), respectively. In this case, there are six bandgaps with different widths, where the third bandgap is the largest and the same as the second omnidirectional bandgap. The second and fifth bandgaps are relatively narrow, which makes it difficult to show a good wave attenuation effect in practical applications, as demonstrated by the transmission spectra in Fig. 7(d). The transmission attenuation coefficients are very small in the third and fourth bandgaps, indicating that the metamaterials have a very strong attenuation effect on elastic wave propagation.

To further investigate the effects of different boundary conditions on the wave attenuation performance as well as the robustness, we calculate the transmission spectra with free boundaries on both sides and find that the transmissions for free boundaries have large fluctuations but the transmissions are obviously decreased in the bandgaps (see Fig. S1 in the supplementary material).

The wave attenuation effects along the ΓX and ΓM directions of the cross-like metamaterials were investigated here. However, the omnidirectional wave attenuation effects of cross-like metamaterials in practical application scenarios need further exploration.

IV. FULL-SCALE TRANSMISSION CALCULATION

In this section, the full-scale transmission calculation model of cross-like metamaterials considering the subway tunnel is built. The wave attenuation effects of cross-like metamaterials on the subway vibration in the transversely isotropic soil are studied in the frequency domain and the time domain.

The full-scale transmission calculation model is shown in Fig. 8. The subway operating tunnel has a diameter of 10 m and a burial depth of 10 m. The parameters of transversely isotropic soil are given in Table I. In the frequency domain calculation, the vibration generated by a running subway train is simulated by applying a vertical linear load to the bottom of the tunnel. The low-reflecting boundary conditions are applied to the left and right sides and the bottom of the model to eliminate the influence of boundary reflections. The cross-like metamaterials are arranged in the subway vibration propagation path with length l_x and depth l_z, and lengths l_1 and l_2 of the cross-like concrete are, respectively, 0.9 and 0.346 m, and the rubber thickness is 2.5 cm. To characterize the wave attenuation effect of the metamaterials, the transmission attenuation coefficient is defined as $20\lg(\Omega_1/\Omega_2)$, where Ω_1 and Ω_2, respectively, represent the total displacement (namely, $\sqrt{|u|^2+|w|^2}$) integral of the black region in Fig. 8 with and without metamaterials.

First, we fix the depth l_z being 15a and study the influence of length l_x on the full-scale transmission of cross-like

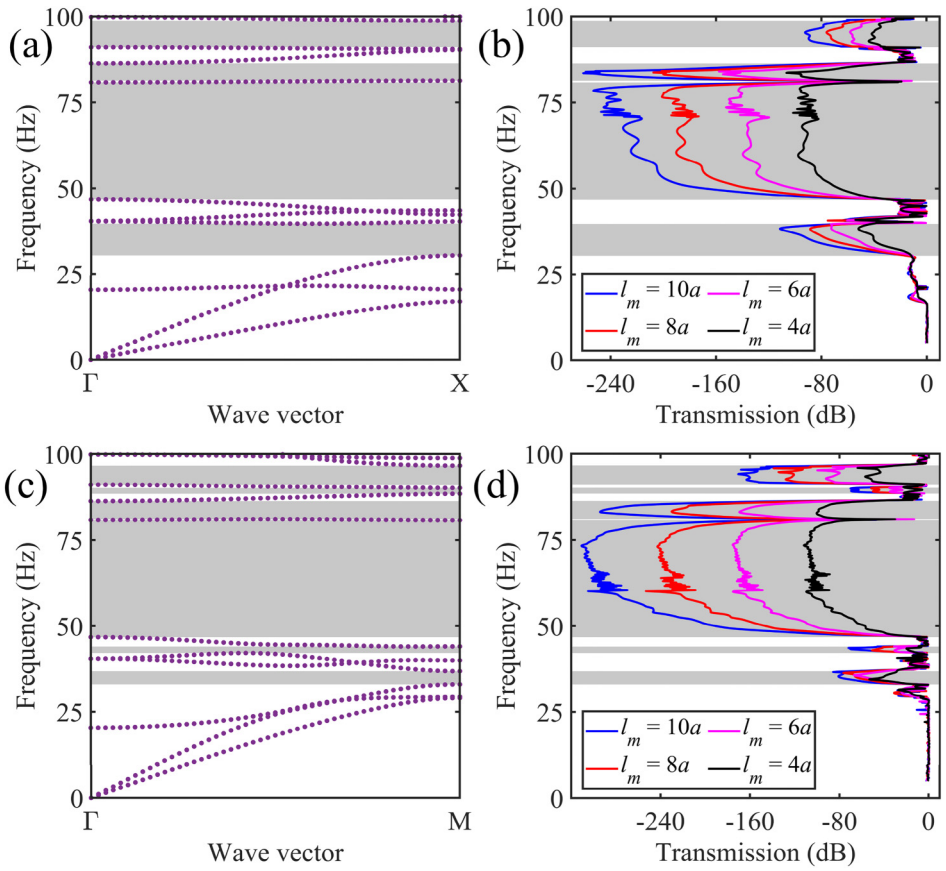

FIG. 7. Band structures along ΓX (a) direction and the corresponding transmission spectra (b). Band structures along the ΓM (c) direction and the corresponding transmission spectra (d).

metamaterials, and the results are shown in Fig. 9(a). One can see that the transmissions decrease significantly in the omnidirectional bandgaps of cross-like metamaterials, which demonstrates the feasibility of metamaterials in practical vibration isolation and attenuation applications. We noticed that the transmissions in bandgaps here are larger than those in Fig. 7. This is because the metamaterial region has a finite size in the full-scale calculation, which leads to a few waves bypassing the metamaterial region, while the transmission model in Fig. 6 is periodic and infinite in the normal incident direction, which implies that no waves can

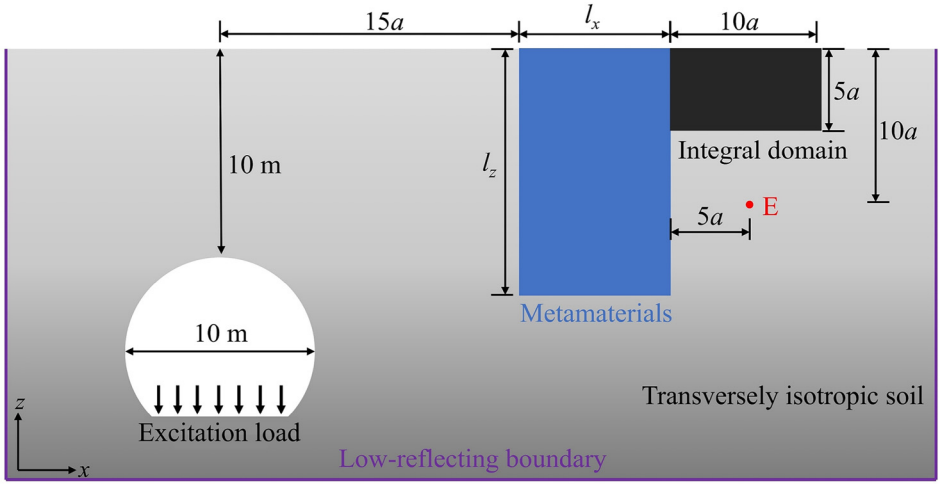

FIG. 8. Full-scale transmission calculation model of metamaterials.

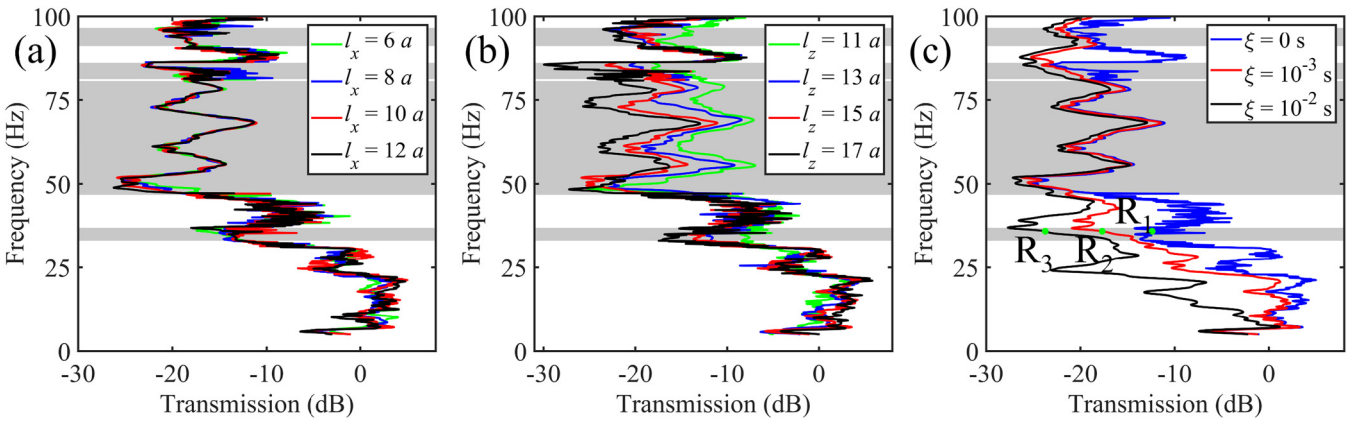

FIG. 9. Full-scale transmission spectra of metamaterials in the frequency domain for different lengths (a), depths (b), and rubber viscosities (c). The gray regions indicate the omnidirectional bandgaps of cross-like metamaterials.

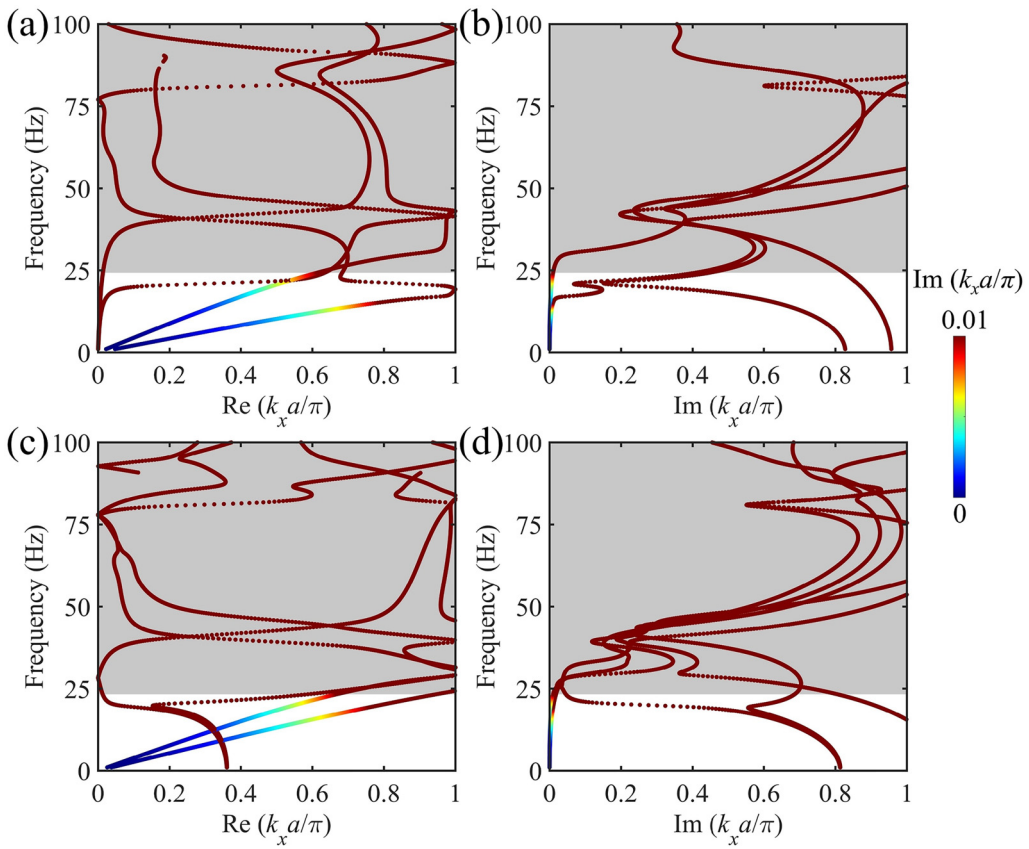

FIG. 10. Real (a) and imaginary (b) parts of the complex band structures of viscoelastic metamaterials along the ΓX direction with rubber viscosity coefficient $\xi = 10^{-3}$ s. Real (c) and imaginary (d) parts of complex band structures of viscoelastic metamaterials along the ΓM direction with rubber viscosity coefficient $\xi = 10^{-3}$ s. The data points are colored according to their imaginary parts. The gray regions indicate the attenuation zones where the imaginary parts are greater than 0.01.

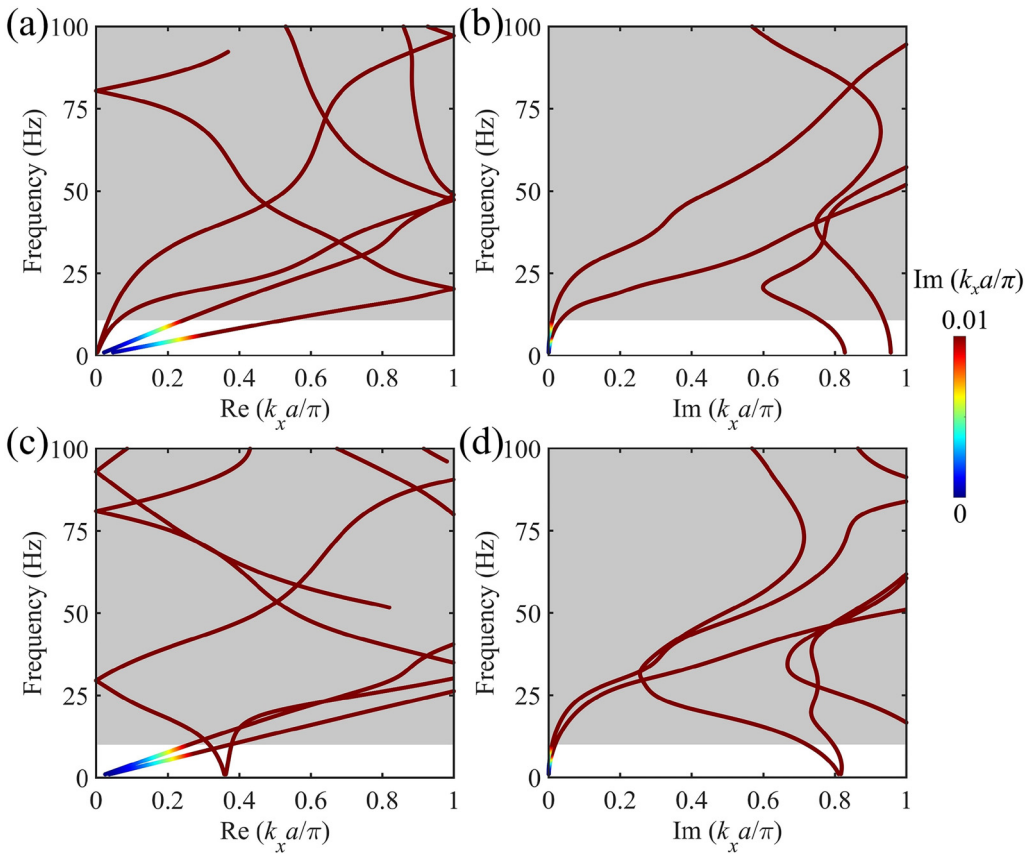

FIG. 11. Real (a) and imaginary (b) parts of the complex band structures of viscoelastic metamaterials along the ΓX direction with rubber viscosity coefficient $\xi = 10^{-2}$ s. Real (c) and imaginary (d) parts of complex band structures of viscoelastic metamaterials along the ΓM direction with rubber viscosity coefficient $\xi = 10^{-2}$ s. The data points are colored according to their imaginary parts. The gray regions indicate the attenuation zones where the imaginary parts are greater than 0.01.

bypass metamaterials. In addition, the transmissions in the passband range between the second and third bandgaps and the third and fourth bandgaps are still small because these bandgaps occupy most of the frequency range, which implies that the wave attenuation performance of the proposed metamaterials is better than expected. The four full-scale transmission spectra with different lengths l_x almost coincide, which illustrates that the length of the metamaterial region has little effect on the wave attenuation. Therefore, the length of the metamaterial region can be appropriately reduced to minimize costs and the occupied space in practical applications.

We next fix the length l_x being $10a$ and study the influence of depth l_z on the full-scale transmission of cross-like metamaterials, and the results are shown in Fig. 9(b). One can see that the transmissions in the bandgaps gradually increase with the decreasing depth l_z. Therefore, the depth of the metamaterial area plays an important role in the wave attenuation effect for underground vibration sources such as subway trains.

The rubber coatings exhibit obvious relaxation in the shear property, i.e., the viscoelastic behavior, which is not considered in the above studies. It is meaningful to investigate the viscous effects of the rubber coatings on the wave attenuation properties of cross-like metamaterials. The Kelvin–Voigt model is used to characterize the rubber viscoelastic behavior, and the shear modulus of rubber is taken as frequency-dependent and expressed as follows:[34]

$$G(\omega) = G_0 - i\omega c = (1 - i\omega\xi)G_0, \tag{8}$$

where G_0 is the elastic shear modulus, c is the dashpot viscosity ,and ξ is the viscosity coefficient defined by $\xi = c/G_0$. We fix the length l_x and depth l_z being $10a$ and $15a$, respectively, and choose three different levels of rubber viscosity coefficient ξ values[30] 0 (elastic), 10^{-3}, and 10^{-2} s to calculate the full-scale transmission of the cross-like metamaterials. The results in Fig. 9(c) indicate that the transmissions in the first bandgap and all passbands decrease with the increasing rubber viscosity, which is favorable to the elastic wave attenuation. The larger rubber viscosity has a significant influence on the low-frequency elastic waves below the second bandgap, as shown by the black line in Fig. 9(c).

To further investigate the effects of the viscosity of rubber on the wave attenuation performance of metamaterials, we calculate

the complex band structures of viscoelastic metamaterials.[48,49] The real and imaginary parts along the ΓX and ΓM directions with rubber viscosity coefficient $\xi = 10^{-3}$ s are shown in Fig. 10. For viscoelastic metamaterials, we need to focus on the minimum imaginary parts to investigate the wave propagation or attenuation properties. We highlight the frequency ranges where the minimum imaginary parts of the wave numbers exceed 0.01 as the effective attenuation zones, which are indicated by the gray regions. We find that the minimum imaginary parts dramatically decrease once the frequency exceeds about 24 Hz, which means that the wave attenuation effects of the viscoelastic metamaterials are enhanced. This phenomenon is consistent with the transmission spectra in Fig. 9(c), where the transmissions of the red curve dramatically decrease after 24 Hz.

The complex band structures of viscoelastic metamaterials along the ΓX and ΓM directions with rubber viscosity coefficient $\xi = 10^{-2}$ s are shown in Fig. 11. Now, the imaginary parts increase in general, and the start frequency of the effective attenuation zone decreases to about 10 Hz. These phenomena are consistent with the transmission spectra in Fig. 9(c), where the transmissions of the black curve dramatically decrease after around 10 Hz.

We show the full-scale wave fields of points R_1, R_2, and R_3 in Fig. 9(c) at different rubber viscosities, as shown in Fig. 12. We notice that most of the vibration energy of the operating subway propagates downward while a small part propagates around. The cross-like metamaterials can prevent wave propagation through them because of the bandgap properties. However, there are still displacement fields with small amplitudes behind metamaterials if we do not consider rubber viscosity, as shown by the light and dark stripes in Fig. 12(a). The displacement amplitudes of wave fields behind the metamaterials gradually reduce with the increasing rubber viscosity due to the dissipative effect of viscoelastic rubber, as demonstrated by the dark blue regions in Figs. 12(b) and 12(c).

To investigate how deviations from idealized conditions might affect the wave attenuation performance of metamaterials, we consider a hole near the metamaterials to introduce boundary irregularities and calculate the transmission spectra of the full-scale model without and with a hole. It is found that the two transmission curves almost coincide (see Fig. S2 in the supplementary material for details).

We further perform the time domain analyses to validate the wave attenuation effect of cross-like metamaterials on the subway vibration. The model of time domain calculation is similar to that of the frequency domain calculation in Fig. 8. Length l_x and depth l_z of the metamaterials are $10a$ and $15a$, respectively. The vertical line displacement is applied to the bottom of the tunnel to simulate the vibration source,

$$W = \begin{cases} A_0(1 - \cos(2\pi f_0 t/n))\sin(2\pi f_0 t), & 0 < t < n/f_0, \\ 0, & t \geq \dfrac{n}{f_0}, \end{cases} \tag{9}$$

where A_0 is the amplitude, f_0 is the central frequency, and n is the number of cycles. In the study, we choose f_0 and n to be 70 Hz and 8, respectively, because the main frequency range of the vibration induced by operating subway trains is about 60–80 Hz,[51] which is located in the bandgaps of the cross-like metamaterials. The model is large enough to prevent boundary reflections of the elastic waves during the studied time. The finite element method is used to perform the time-dependent calculation with the time step being $1/(30f_0)$. The displacement components u and w of point E (shown in Fig. 8) after metamaterials are detected to characterize the wave attenuation effect.

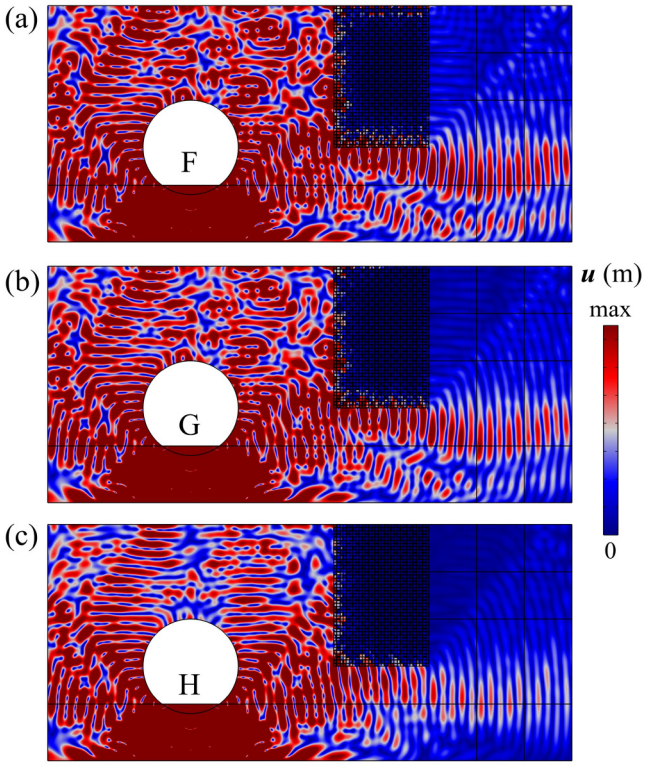

FIG. 12. Full-scale wave fields of points R_1 (a), R_2 (b), and R_3 (c) in Fig. 8(c) at 25.8 Hz with different rubber viscosities.

The detected signals in the time domain of the displacement component u without and with metamaterials are shown in Fig. 13(a). One can see that the amplitudes of the signals with metamaterials decrease significantly compared to those without metamaterials. The corresponding frequency spectra via the fast Fourier transform are shown in Fig. 13(b). It is noticed that the excited elastic waves mainly cover the frequency range of about 60–80 Hz, as indicated by the blue line. The normalized amplitudes in the presence of the metamaterials are much smaller than in their absence, which demonstrates the great wave attenuation effect of the cross-like metamaterials. In addition, similar results are found for the displacement component w, as illustrated in Figs. 13(c) and 13(d).

V. INFLUENCES OF GEOMETRIC PARAMETERS

In this section, the influences of geometric parameters of rubber thickness t and parameter l_3 on the omnidirectional

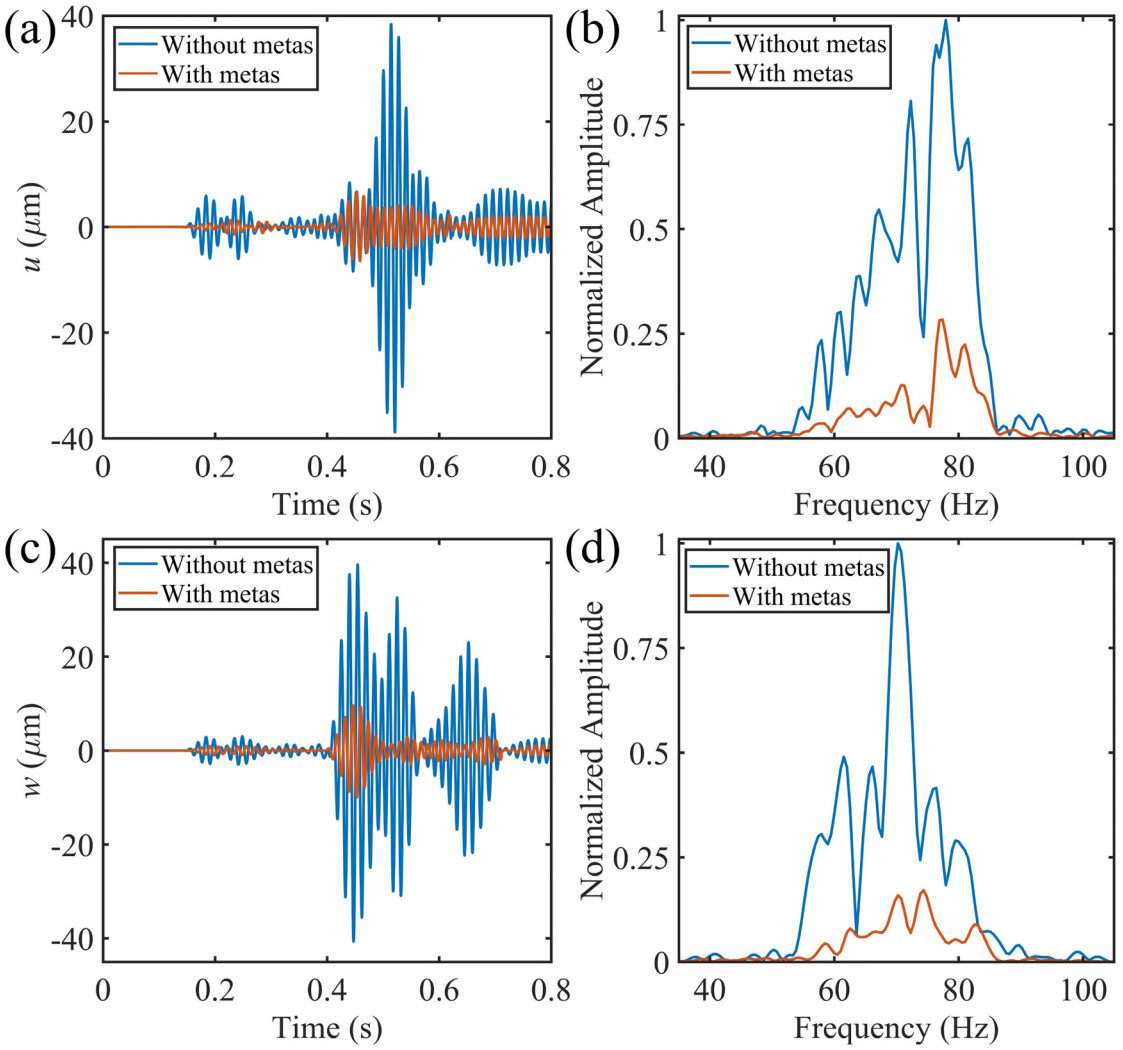

FIG. 13. The detected signals of the *x*-direction displacement component *u* of point E in Fig. 8 in the time domain (a) and the corresponding frequency spectra (b). The detected signals of the *z*-direction displacement component *w* of point E in Fig. 8 in the time domain (c) and the corresponding frequency spectra (d).

bandgaps of the cross-like metamaterials are investigated. Then, the solid concrete is replaced by the hollow concrete to study the bandgap variations.

The variation of omnidirectional bandgaps with rubber thickness *t* is shown in Fig. 14(a). For the first, third, and fourth bandgaps, their central frequencies and widths gradually decrease with the increasing rubber thickness. This results from the thicker rubber thickness leading to a lower resonant frequency of the rubber-concrete element. However, the width of the second bandgap manifests increase with the increasing rubber thickness, where the lower edge frequency decreases fast and quasilinearly while the upper one decreases slightly. The second bandgap occupies the frequency range of about 40–80 Hz when the rubber thickness is 3 cm. Therefore, the rubber thickness plays an important role in the bandgap properties of the proposed cross-like metamaterials.

The parameter l_3 has a significant impact on the omnidirectional bandgaps of the cross-like metamaterials, as shown in Fig. 14(b). The first bandgap widens with the increasing parameter l_3, where the lower and upper edge frequencies, respectively, decrease and increase. The second bandgap width first increases and then decreases, while the third bandgap width decreases to 0 and then increases. The upper edges of the second and third bandgaps interchange when parameter l_3 is greater than 40 cm. The fourth bandgap width first increases and then decreases to 0 with the increasing parameter l_3. Changing l_3 affects not only the filling ratio of the concrete but also the local resonance effects of the rubber-concrete element and square soils connected by the narrow

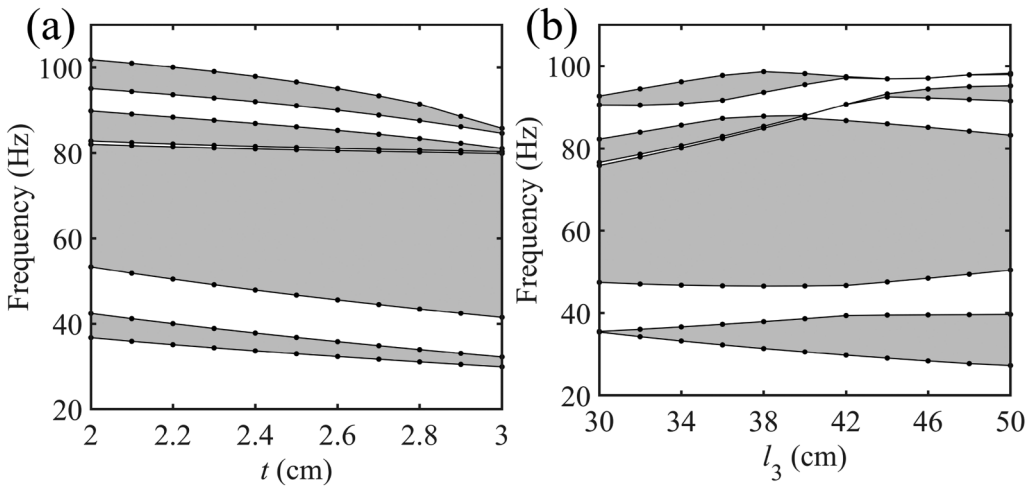

FIG. 14. Variation of omnidirectional bandgaps with rubber thickness t (a) and geometric parameter l_3 (b).

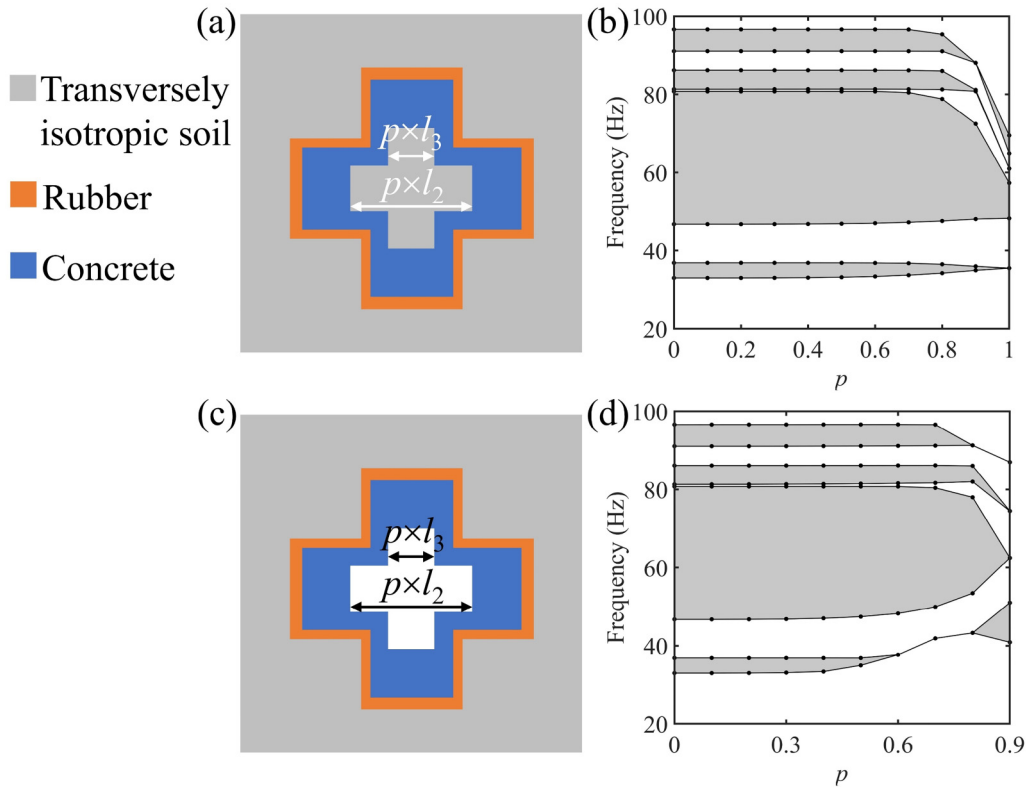

FIG. 15. Hollow concrete with filled soil (a) and the corresponding variation of omnidirectional bandgaps with parameter p (b). Hollow concrete without filled soil (c) and the corresponding variation of omnidirectional bandgaps with parameter p (d).

connectors, which has an impact on the bandgaps. These results imply that geometric parameters are crucial for the bandgap properties of metamaterials, which could be used to design the bandgap frequency ranges of metamaterials based on practical demand.

To reduce the construction costs, we further study the bandgap properties of the cross-like metamaterials with hollow concrete, and the hollow is cross-like with the geometric parameters being p times ($0 \le p \le 1$) those of the solid concrete. First, we consider the hollow concrete with filled soil as shown in Fig. 15(a), and the corresponding variation of the omnidirectional bandgaps with parameter p is summarized in Fig. 15(b). When p is smaller than 0.6, the bandgaps remain unchanged. The filling ratio of the hollow concrete is 0.64 times that of the solid concrete when p is 0.6. However, the four bandgaps narrow sharply when p is greater than 0.8. Consequently, we can utilize hollow concrete with filled soil of appropriate geometric parameters to reduce the construction costs. For the hollow concrete without filled soil shown in Fig. 15(c), the corresponding results are summarized in Fig. 15(d). Now, the bandgaps remain unchanged until p is 0.4. Then, the first bandgap vanishes and reappears with the increasing parameter p. However, the first bandgap for the larger parameter p is not the same one as for the smaller parameter p. The other three bandgaps narrow sharply when p is greater than 0.8.

VI. CONCLUSIONS

In summary, we presented a comprehensive investigation of omnidirectional bandgaps and wave attenuation properties of cross-like metamaterials in transversely isotropic soil. Compared to circle and square metamaterials, the proposed cross-like metamaterials have more and wider bandgaps, where the second bandgap is quite large with a normalized bandgap width of 53.5% and almost connected with the third bandgap. Interestingly, the larger anisotropy of soil would facilitate the opening and widening of the bandgaps of the cross-like metamaterials. The transmission spectra of cross-like metamaterials along the ΓX and ΓM directions were calculated to demonstrate the wave attenuation effect of directional bandgaps. Furthermore, the full-scale transmission calculations of the cross-like metamaterials considering the subway vibration were conducted in the frequency and time domains. The full-scale transmissions decrease significantly in the omnidirectional bandgaps of the cross-like metamaterials, supporting the feasibility of metamaterials in practical applications. In addition, we found that for underground vibration sources, a larger depth of the metamaterial region could enhance the wave attenuation performance. In addition, considering rubber viscosity would enhance the wave attenuation in the overall frequency ranges and lower the start frequency of the attenuation zones. Finally, the variations of omnidirectional bandgaps with rubber thickness and geometric parameters were studied, which shows the designability and flexibility of cross-like metamaterials. We further showed that the hollow concrete without and with filled soil could replace the solid concrete to reduce costs without changing the bandgaps when the hollow size is less than a certain critical value. In conclusion, the main novel contribution of this work is that we propose a locally resonant and cross-like metamaterial to achieve broadband attenuation for omnidirectional bulk waves in transversely isotropic soil. The cross-like shape and rubber coating are important for the bandgap opening and variations, which can be designed to achieve the desired bandgaps. The other important finding is that the proposed cross-like metamaterials have better wave attenuation performance in the soil with larger anisotropy, which has not been reported to our knowledge. Our work may open promising avenues for designing and optimizing metamaterials with omnidirectional wave attenuation performance in transversely isotropic soil. It also provides reference and guidance for the practical applications of metamaterials in vibration reduction and isolation for subway or other underground vibrations.

SUPPLEMENTARY MATERIAL

See the supplementary material for the effects of the boundary conditions and boundary irregularities on the wave attenuation performance.

ACKNOWLEDGMENTS

This work was supported by the National Natural Science Foundation of China (NNSFC) (No. 52278411), the National Natural Science Foundation of China (NNSFC) (No. 12272267), the Young Elite Scientists Sponsorship Program by CAST (No. 2021QNRC001), the Shanghai Science and Technology Commission (Grant No. 22JC1404100), and the Shanghai Gaofeng Project for University Academic Program Development. The first author is grateful for the support of the China Scholarship Council (Grant No. 202206260205). This work is a part of the project MAGNIFIC, which has received funding from the European Union's Horizon Europe research and innovation program under Grant Agreement No. 101091968. The project was also supported by the French National Research Agency ANR under Grant Agreement No. ANR-19-CE24-0014.

AUTHOR DECLARATIONS

Conflict of Interest

The authors have no conflicts to disclose.

Author Contributions

Runcheng Cai: Conceptualization (equal); Data curation (equal); Formal analysis (equal); Investigation (equal); Methodology (equal); Software (equal); Validation (equal); Visualization (equal); Writing – original draft (equal); Writing – review & editing (equal). **Yabin Jin:** Conceptualization (equal); Data curation (equal); Formal analysis (equal); Funding acquisition (equal); Investigation (equal); Methodology (equal); Project administration (equal); Resources (equal); Software (equal); Supervision (equal); Validation (equal); Visualization (equal); Writing – original draft (equal); Writing – review & editing (equal). **Yan Pennec:** Conceptualization (equal); Formal analysis (equal); Investigation (equal); Methodology (equal); Resources (equal); Validation (equal); Visualization (equal); Writing – original draft (equal); Writing – review & editing (equal). **Bahram Djafari-Rouhani:** Formal analysis (equal); Investigation (equal); Methodology (equal); Resources (equal); Supervision (equal); Validation (equal);

Visualization (equal); Writing – original draft (equal); Writing – review & editing (equal). **Timon Rabczuk:** Formal analysis (equal); Investigation (equal); Methodology (equal); Software (equal); Validation (equal); Visualization (equal); Writing – original draft (equal); Writing – review & editing (equal). **Xiaoying Zhuang:** Conceptualization (equal); Data curation (equal); Formal analysis (equal); Funding acquisition (equal); Investigation (equal); Methodology (equal); Project administration (equal); Resources (equal); Software (equal); Supervision (equal); Validation (equal); Visualization (equal); Writing – original draft (equal); Writing – review & editing (equal).

DATA AVAILABILITY

The data that support the findings of this study are available from the corresponding authors upon reasonable request.

REFERENCES

[1]S. Amanat, R. Rafiee-Dehkharghani, M. Bitaraf, and D. Bansal, Int. J. Eng. Sci. **173**, 103655 (2022).
[2]M.-H. Lu, L. Feng, and Y.-F. Chen, Mater. Today **12**, 34 (2009).
[3]S. A. Cummer, J. Christensen, and A. Alù, Nat. Rev. Mater. **1**, 1 (2016).
[4]G. Ma and P. Sheng, Sci. Adv. **2**, e1501595 (2016).
[5]Y. Jin, Y. Pennec, B. Bonello, H. Honarvar, L. Dobrzynski, B. Djafari-Rouhani, and M. I. Hussein, Rep. Prog. Phys. **84**, 086502 (2021).
[6]H. K. Zhang, Y. Chen, X. N. Liu, and G. K. Hu, J. Mech. Phys. Solids **135**, 103796 (2020).
[7]X. Li, Y. Chen, R. Zhu, and G. Huang, Mech. Syst. Signal Process. **149**, 107324 (2021).
[8]Z. Lin, H. Ramezani, T. Eichelkraut, T. Kottos, H. Cao, and D. N. Christodoulides, Phys. Rev. Lett. **106**, 213901 (2011).
[9]X. Wu, Z. Wen, Y. Jin, T. Rabczuk, X. Zhuang, and B. Djafari-Rouhani, Int. J. Mech. Sci. **205**, 106592 (2021).
[10]Y. Jin, S. Zeng, Z. Wen, L. He, Y. Li, and Y. Li, Mater. Des. **215**, 110499 (2022).
[11]W. Gao, Z. Qin, and F. Chu, Int. J. Mech. Sci. **228**, 107485 (2022).
[12]H. Xue, Y. Yang, and B. Zhang, Nat. Rev. Mater. **7**, 974 (2022).
[13]A. Ni and Z. Shi, Eng. Struct. **262**, 114378 (2022).
[14]W. Wang, Y. Jin, W. Wang, B. Bonello, B. Djafari-Rouhani, and R. Fleury, Phys. Rev. B **101**, 024101 (2020).
[15]Y. Jin, W. Li, B. Djafari-Rouhani, Y. Li, and Y. Xiang, J. Sound Vib. **572**, 118162 (2024).
[16]R. Cai, Y. Jin, Y. Li, T. Rabczuk, Y. Pennec, B. Djafari-Rouhani, and X. Zhuang, Phys. Rev. Appl. **18**, 014067 (2022).
[17]R. Cai, Y. Jin, Y. Li, J. Zhu, H. Zhu, T. Rabczuk, and X. Zhuang, J. Sound Vib. **555**, 117710 (2023).
[18]M. I. Rosa, M. Mazzotti, and M. Ruzzene, J. Mech. Phys. Solids **149**, 104325 (2021).
[19]R. Cai, Y. Jin, T. Rabczuk, X. Zhuang, and B. Djafari-Rouhani, J. Appl. Phys. **129**, 124903 (2021).
[20]Muhammad, C. W. Lim and K. Kamil Żur, Eng. Struct. **246**, 113019 (2021).
[21]C. Cai, L. Gao, X. He, Y. Zou, K. Yu, and D. Wu, Comput. Geotech. **139**, 104421 (2021).
[22]T. Li, Q. Su, and S. Kaewunruen, Constr. Build. Mater. **260**, 119936 (2020).
[23]Y. M. Luo, C. He, Z. Tao, J. Hao, H. H. Xu, Y. Zhang, F. Zhang, and X. Ren, Int. J. Mech. Sci. **262**, 108715 (2024).
[24]X. Pu and Z. Shi, J. Sound Vib. **468**, 115130 (2020).
[25]X. Wu, Y. Jin, A. Khelif, X. Zhuang, T. Rabczuk, and B. Djafari-Rouhani, Mech. Adv. Mater. Struct. **29**, 1 (2021).
[26]Y. Zeng, Y. Xu, K. Deng, P. Peng, H. Yang, M. Muzamil, and Q. Du, J. Appl. Phys. **125**, 224901 (2019).
[27]Z. Chen, G. Wang, and C. Lim, Eng. Struct. **276**, 115375 (2023).
[28]Y. Jiang, F. Meng, Y. Chen, Y. Zheng, X. Chen, J. Zhang, and X. Huang, Comput. Geotechn. **128**, 103821 (2020).
[29]L. Meng, Z. Cheng, and Z. Shi, Comput. Geotechn. **117**, 103251 (2020).
[30]L. Meng, Z. Cheng, and Z. Shi, Comput. Geotechn. **124**, 103633 (2020).
[31]C. X. Liu and G. L. Yu, Comput.-Aided Civil Infrastruct. Eng. **37**, 451 (2022).
[32]A. Gupta, R. Sharma, A. Thakur, and P. Gulia, Sci. Rep. **13**, 2293 (2023).
[33]F. Basone, O. S. Bursi, F. Aloschi, and G. Fischbach, Sci. Rep. **11**, 9728 (2021).
[34]R. Cai, Y. Jin, B. Djafari-Rouhani, S. Zhou, P. Chen, T. Rabczuk, H. Zhu, and X. Zhuang, Comput. Geotech. **165**, 105854 (2024).
[35]X. Pu and Z. Shi, Constr. Build. Mater. **180**, 177 (2018).
[36]L. Wu and Z. Shi, Soil Dyn. Earthq. Eng. **156**, 107213 (2022).
[37]Y. Chen, F. Qian, F. Scarpa, L. Zuo, and X. Zhuang, Mater. Des. **175**, 107813 (2019).
[38]X. Pu, A. Palermo, Z. Cheng, Z. Shi, and A. Marzani, Int. J. Eng. Sci. **154**, 103347 (2020).
[39]Z. Y. Ai, J. J. Yang, and H. T. Li, Appl. Math. Model. **75**, 865 (2019).
[40]Z. Y. Ai and G. P. Ren, Soil Dyn. Earthq. Eng. **83**, 162 (2016).
[41]Z. Y. Ai, Z. X. Li, and N. R. Cang, Soil Dyn. Earthq. Eng. **60**, 22 (2014).
[42]D.-X. Ji and G.-L. Yu, Proc. Inst. Mech. Eng. Pt. L **236**, 2242 (2022).
[43]D.-K. Guo and T. Chen, Mater. Today Commun. **28**, 102526 (2021).
[44]K. Zhang, J. Luo, F. Hong, and Z. Deng, Eng. Struct. **232**, 111870 (2021).
[45]Y.-F. Wang, Y.-S. Wang, and X.-X. Su, J. Appl. Phys. **110**, 113520 (2011).
[46]Y.-F. Wang and Y.-S. Wang, J. Sound Vib. **332**, 2019 (2013).
[47]J. Huang and Z. Shi, Int. J. Geomech. **13**, 132 (2013).
[48]F. Aloschi, O. S. Bursi, A. Palermo, and A. Marzani, Int. J. Mech. Sci. **269**, 109054 (2024).
[49]F. Aloschi, R. Andreotti, and O. S. Bursi, Sci. Rep. **13**, 6510 (2023).
[50]J.-J. Liao and C. D. Wang, Int. J. Numer. Anal. Methods Geomech **22**, 425 (1998).
[51]C.-X. Liu and G.-L. Yu, Eng. Struct. **277**, 115441 (2023).